GaInAsP/silicon-on-insulator hybrid laser with ring-resonator-type reflector fabricated by N_2 plasma-activated bonding

2016 Jpn. J. Appl. Phys. 55 082701

(http://iopscience.iop.org/1347-4065/55/8/082701)

Japanese Journal of Applied Physics **55**, 082701 (2016)
http://doi.org/10.7567/JJAP.55.082701

REGULAR PAPER

GaInAsP/silicon-on-insulator hybrid laser with ring-resonator-type reflector fabricated by N_2 plasma-activated bonding

Yusuke Hayashi[1]*, Junichi Suzuki[1], Satoshi Inoue[1], Shovon Muhammad Tanvir Hasan[1], Yuki Kuno[1], Kazuto Itoh[1], Tomohiro Amemiya[1,2], Nobuhiko Nishiyama[1,2], and Shigehisa Arai[1,2]

[1]*Department of Electrical and Electronic Engineering, Tokyo Institute of Technology, Meguro, Tokyo 152-8552, Japan*
[2]*Institute of Innovative Research, Tokyo Institute of Technology, Meguro, Tokyo 152-8552, Japan*

*E-mail: hayashi.y.ao@m.titech.ac.jp

Received April 12, 2016; accepted May 16, 2016; published online July 19, 2016

III–V/Si hybrid integration with direct bonding is an attractive method of realizing an electrophotonic convergence router with a small size and a low power consumption. Plasma-activated bonding (PAB) is an effective approach for reducing thermal stress during the bonding process because PAB achieves a high bonding strength with low-temperature annealing. This time, the fabrication of a GaInAsP/silicon-on-insulator (SOI) hybrid laser with Si ring-resonator-type reflectors was demonstrated by N_2 PAB. By measuring the lasing spectra, we confirmed the reflective characteristics resulting from the cascaded Si ring resonators. We also investigated kink characteristics, which occur around the threshold current, of the current–light output (*I–L*) characteristics, and successfully approximated the kink characteristics by considering saturable absorption occurring at the III–V/Si taper tip. The taper structure was investigated in terms of a passive device as well as an active device, and a structure for eliminating saturable absorption was proposed.

1. Introduction

The demand for high-efficiency and large-capacity optical network systems has been increasing owing to the rapidly growing volume of Internet traffic, and the transmission bandwidth is becoming a bottleneck in large-scale data centers or in supercomputing systems.[1,2] In recent years, optical interconnects implemented in high-end routers have established optical-fiber links between multiple linecards within the router chassis.[3,4] Such new-generation routing systems are expected to achieve not only a high transmission bandwidth but also savings in system size and power consumption.

As a platform to more closely combine signal processing based on the electrical domain and signal routing based on the optical domain, Si photonics has gained attention owing to its compatibility with Si CMOS fabrication processes[5–7] as well as its high-density integration ability based on a large refractive index contrast between the Si core and the SiO_2 cladding.[8,9] In recent years, Si photonics technology has been applied to chip-to-chip interposers in place of conventional electrical bus systems.[10–12] Consequently, a high-density transmission of 30 Tbps/cm^2 has been demonstrated.[13]

However, producing radiative emissions from bulk Si is almost impossible because it is an indirect bandgap semiconductor, presenting a large barrier for the integration of monolithic light sources. Therefore, it is currently a realistic option to integrate an optical gain medium, such as III–V-based gain materials, into photonic integrated circuits (PICs) fabricated on the basis of Si photonics.

III–V/Si hybrid integration using direct bonding technologies[14–17] is emerging as a platform for large-scale PICs, wherein conventional III–V-based PIC technology is combined with Si photonics technology. Furthermore, wafer-to-wafer bonding is particularly superior for mass productivity compared with flip-chip assembly, because a large number of gain sections can be formed simultaneously during a single bonding process. Such advantages are appropriate for implementing a photonics–electronics convergence router in one chip, as several router devices (such as an in-line amplifier, a monitor, a wavelength-tunable laser, and a wavelength converter) must be composed of III–V-based materials and formed in various places on a Si passive circuit. Among these router devices, a tunable laser, as a part of a wavelength conversion system, is a key element in forming a wavelength-convertible network.[18,19] Recently, by using low-loss Si waveguides and ring resonators as an external cavity, tunable lasers that exhibit a sub mode suppression ratio (SMSR) of more than 45 dB across a tunable wavelength range of 54 nm, an SMSR of more than 29 dB across a tunable range of 99 nm, and a linewidth of less than 15 kHz across the C-band have been realized.[20–22]

Various III–V/Si hybrid devices fabricated by heterogeneous integration, such as hydrophilic bonding,[23–25] hydrophobic bonding,[26,27] metal bonding,[28,29] oxygen-plasma-assisted bonding,[30–34] adhesive bonding,[35–38] and flip-chip assembly,[22,39] have been reported. Our group has also reported distributed feedback (DFB) lasers with wirelike active regions, prepared by hydrophilic bonding.[40–42] However, this bonding method needs a relatively high bonding temperature that may cause damage to wafers because of thermal stress from the difference between the thermal expansion coefficients of InP and Si. We introduced a low-temperature bonding method with N_2 plasma activation.[14,15] Owing to this low-temperature bonding at 150 °C, we achieved a relatively low threshold current density J_{th} of 850 A/cm^2 (170 A/cm^2/well) on a bare SOI substrate.[16]

Referring to previous results obtained by N_2 plasma-activated bonding (PAB), in this paper, we report on the investigation of a hybrid laser using Si ring resonators, aiming at the implementation of a photonics–electronics convergence router. Several wavelength-tunable lasers exhibiting a high SMSR, a wide tunable range or a narrow linewidth based on Si photonics technology have already been reported. Our goals are to combine such a prominent wavelength selectivity with the low-temperature integration method of N_2 PAB and to improve fundamental lasing characteristics such as threshold current and external differential quantum efficiency.

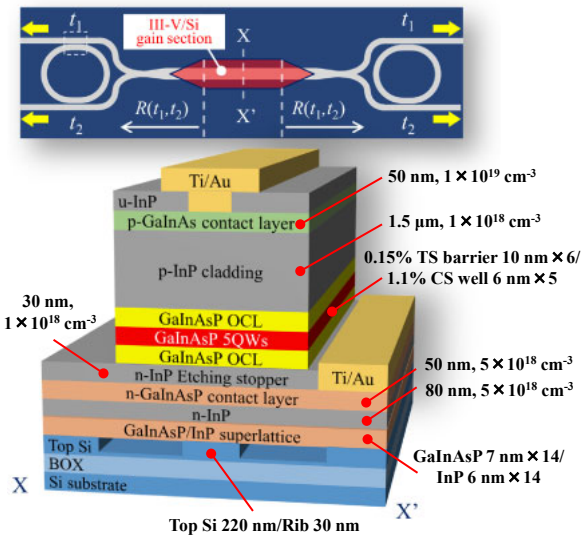

Fig. 1. (Color online) Top view and cross-sectional view of fabricated hybrid lasers. t_1 and t_2 represent the transmission coefficients between the ring resonator and the bus waveguide. $R(t_1, t_2)$ represents reflectivity at the ring-resonator-type reflector. The cross-sectional view at the X–X′ line shows the layer structure of the III–V/Si gain section.

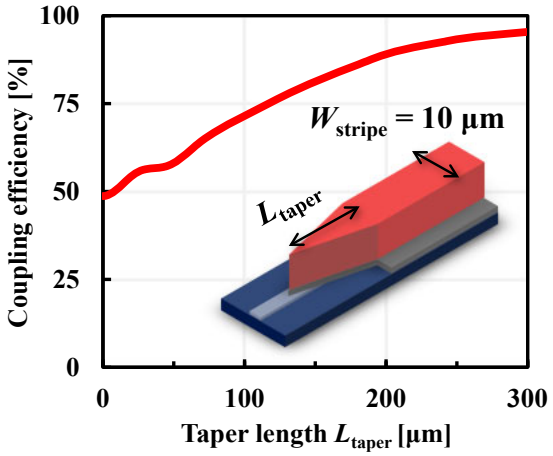

Fig. 2. (Color online) Calculation result of coupling efficiency in III–V/Si taper. The coupling efficiency of −1 dB (79%) was estimated at a taper length of 140 μm.

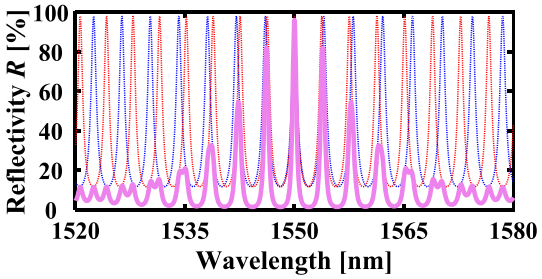

Fig. 3. (Color online) Reflective characteristics of ring-resonator-type reflectors. Two cascading rings showing FSRs of 4.01 nm (blue) and 3.74 nm (red) enable an FSR of 55.5 nm (purple).

In Sect. 2, we consider the design of the laser, focusing on the ring-resonator-type reflector and III–V/Si taper. In Sect. 3, the device fabrication and measurement results are described, and in Sect. 4, we discuss the cause of the kink characteristics seen in the current–light output (*I*–*L*) characteristics and suggest how such kink characteristics can be improved. The III–V/Si taper structure is investigated in terms of a passive device as well as an active device, and a novel structure for removing saturable absorption is proposed. In Sect. 5, the experimental results, discussions, and future outlook are summarized.

2. Design of III–V/Si hybrid devices

We considered a structure where ring-resonator-type reflectors were placed on both sides of the III–V/Si gain section, as shown in Fig. 1, while the III–V gain region was directly bonded on an SOI wafer. Five-layer GaInAsP quantum wells (QWs) consisting of a 1.1% compressively strained (CS) well, a 0.15% tensile-strained (TS) barrier, and an optical confinement layer (OCL) were used for the active region. A 14-period GaInAsP (7 nm)/InP (6 nm) superlattice was introduced to compensate for the thermal stress caused by the direct bonding process.[43] On the SOI wafer surface, Si rib waveguides (waveguide height: 220 nm, rib height: 30 nm) were patterned by electron beam lithography.

The taper structure was introduced between the III–V/Si gain and Si waveguide sections to achieve adiabatic mode coupling. Several groups have numerically and experimentally demonstrated highly efficient mode coupling in the III–V/Si taper by varying the length, width or tip width of the taper structure.[25,37,44–47] In terms of mode coupling, a thick Si waveguide (>500 nm) is preferable because a thin Si waveguide (<400 nm) causes a large difference in the mode shape compared with that of a III–V/Si waveguide.[37] Nevertheless, we adopted a 220-nm-thick Si waveguide that exhibits the advantages of structural compatibility with other Si photonic devices as well as a high optical confinement ability in the gain region. Because, so far, Si waveguide thicknesses from 300 to 700 nm have mainly been investigated in the previous studies, the mode coupling efficiency in our structure with a 220-nm-thick Si waveguide (Fig. 1) was examined here. Figure 2 shows the coupling efficiency calculated by combining the finite difference method (FDM) and the eigen mode expansion (EME) method. An inverse tapered structure was formed between a 10-μm-wide III–V stripe and a 2-μm-wide Si waveguide to couple each fundamental mode. The coupling efficiency of −1 dB (79%) was estimated at a taper length of 140 μm, which can be patterned by photolithography. Thus, various taper structures with lengths of 50, 100, and 150 μm are demonstrated, as described in Sect. 3, and their coupling efficiencies are compared.

We also estimated the characteristics of a laser based on a ring-resonator-type reflector. The high-Q resonance and Vernier effect of the Si ring resonators can generate a high SMSR. Figure 3 shows the reflectivity R of cascaded ring resonators in the case of $t_1 = t_2 = 0.7$. Here, t represents the electric field transmission coefficient between the ring resonator and the bus waveguide, and R represents the power reflectivity. Identical transmission coefficients of t_1 and t_2 are used in both ring resonators. The free spectral range (FSR) of each ring resonator was set as $\Delta\lambda_1 = 4.01$ nm and $\Delta\lambda_2 = 3.74$ nm, and this condition is estimated to result in an FSR of 56 nm via the Vernier effect.

Figure 4 shows the reflectivity and SMSR of the cascaded ring reflectors in the case of varying the transmission

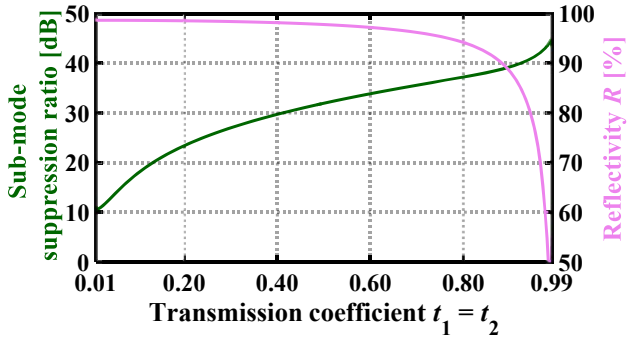

Fig. 4. (Color online) Calculation results of reflectivity and SMSR of ring-resonator-type reflectors in the case of $t_1 = t_2$.

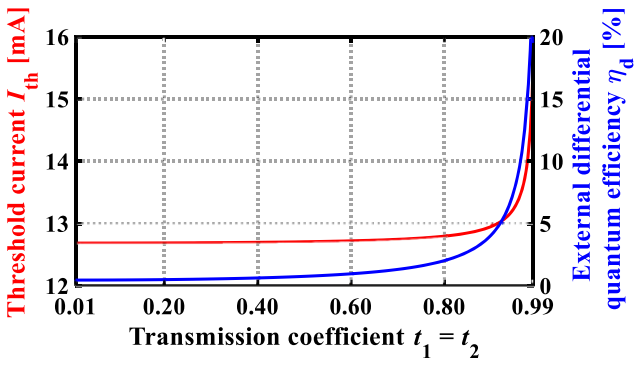

Fig. 5. (Color online) Calculation results of I_{th} and η_d in the case of $t_1 = t_2$.

Table I. Values used in the calculation of laser characteristics.

Active region length L_{act} (mm)	1
Active region width W_{act} (μm)	3.6
Internal quantum efficiency η_i (%)	70
Propagation loss of active region α_{act} (cm^{-1})	10
Propagation loss of Si waveguide α_{Si} (cm^{-1})	0.92
Optical confinement factor ξ_{QW} (%)	4.8
Effective spontaneous recombination coefficient B_{eff} (cm^3/s)	1.5×10^{-10}
Transparency carrier density N_g (cm^{-3})	1.5×10^{18}
Differential gain $\partial g/\partial N$ (cm^2)	6×10^{-16}

coefficient.[48] Reflectivity decreases as transmission coefficient increases. This is because a high transmission coefficient leads to strong resonances of light and increments in propagation loss. For example, a reflectivity of 96% and an SMSR of 35 dB can be obtained in the case of $t_1 = t_2 = 0.7$. The threshold current I_{th} and external differential quantum efficiency η_d can also be controlled by the transmission coefficients, as shown in Fig. 5. The calculations of I_{th} and η_d are based on variables listed in Table I.[49] I_{th} and η_d are found to increase steeply with a high transmission coefficient exceeding 0.8 because in the steep variation of reflectivity. In the first demonstration, we used a design with $t_1 = t_2 = 0.7$ to achieve a high SMSR and a low threshold current of 13 mA. Details are described in the following section. Note that a high-reflectivity design is not suitable for the extraction of light from a laser. In this case, η_d was estimated to be only 1.3% because light is strongly confined in the ring resonators. In order to reduce reflectivity and enhance η_d, varying t_1 and

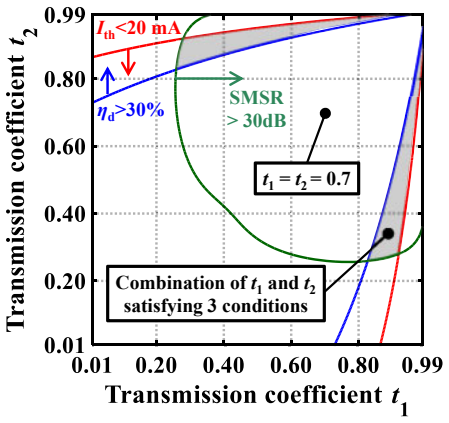

Fig. 6. (Color online) Overlap of three conditions required to achieve laser performance of $I_{th} < 20$ mA, $\eta_d > 30\%$, and SMSR > 30 dB. Gray areas indicate the combination of t_1 and t_2 satisfying these conditions simultaneously.

t_2 independently is effective as shown in Fig. 6. It is possible to design a ring resonator such that η_d increases greatly while I_{this} unchanged to some extent. For example, the laser performance of $I_{th} < 20$ mA, $\eta_d > 30\%$, and SMSR > 30 dB at a taper length of 140 μm can be achieved simultaneously if the combination of t_1 and t_2 satisfies the three conditions.

3. Fabrication and measurement of hybrid laser

We fabricated hybrid lasers based on the design described in the previous section. The schematics and scanning electron microscopy (SEM) images of the fabricated lasers are shown in Fig. 7. We chose the design of a symmetric ring resonator with the coupling of $t_1 = t_2 = 0.7$, where all couplers connecting a ring resonator and a waveguide were identically designed to simplify the structure.

The fabrication process is as follows. First, an SOI wafer and an InP wafer were prepared for a direct bonding process. On the SOI wafer surface, Si rib waveguides of 220 nm waveguide height and 30 nm rib height were patterned. Moreover, the GaInAsP/InP multiple-quantum-well structure shown in Table I (the actual order of epitaxial growth is the reverse of this table) was grown on an n-InP substrate by organometallic vapor-phase epitaxy (OMVPE). Then, the SOI and InP wafers were directly bonded by N_2 plasma activation.[15] Maintaining a high vacuum state ($\sim 10^{-4}$ Pa) from plasma irradiation to temporary bonding prevents the oxidization or contamination of the wafer surface,[50] consequently enabling wafer bonding at a low temperature. To activate the surfaces of the SOI and InP wafers, N_2 plasma was irradiated for 10 s. After that, the two wafers were bonded under 250 kPa pressure for 2 h while ramping up the chamber temperature from room temperature to 150 °C.

After the bonding, the n-InP substrate and GaInAs etch-stop layer were removed by wet etching. Next, III–V stripe patterns for the gain section were formed by etching the epitaxial layers until the n-InP etch-stop layer was exposed below the active layers. Subsequently, island patterns were formed by etching off all the III–V layers from the Si waveguide surface. Then, a 1-μm-thick SiO_2 cladding was deposited by plasma-enhanced chemical-vapor deposition (PECVD), and windows were opened on the III–V islands to form p/n electrodes. The window opening of the SiO_2

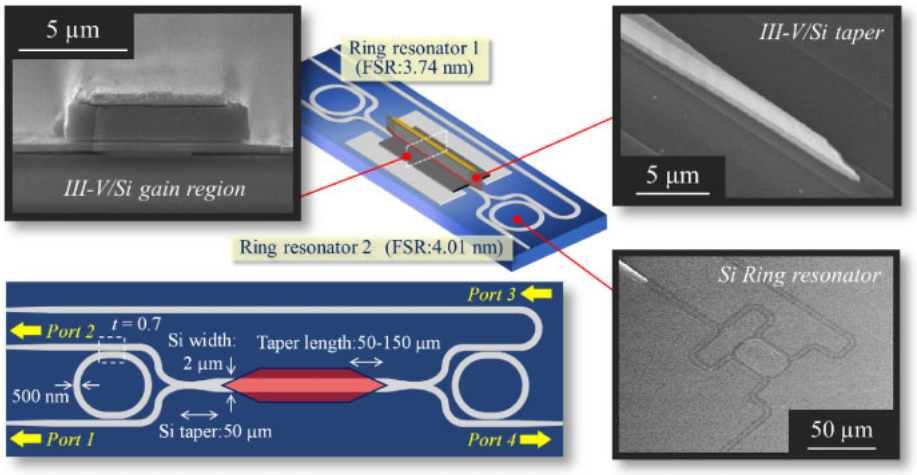

Fig. 7. (Color online) Schematics and SEM images of fabricated laser. The top left SEM image shows the cross-sectional view of the gain section, where the Si waveguide can be seen under the III–V stripe. Top right and bottom right SEM images show the top view of the taper section and the Si ring resonator.

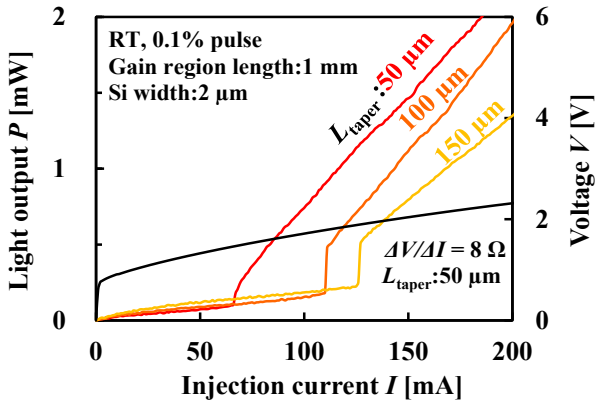

Fig. 8. (Color online) Lasing characteristics of hybrid lasers.

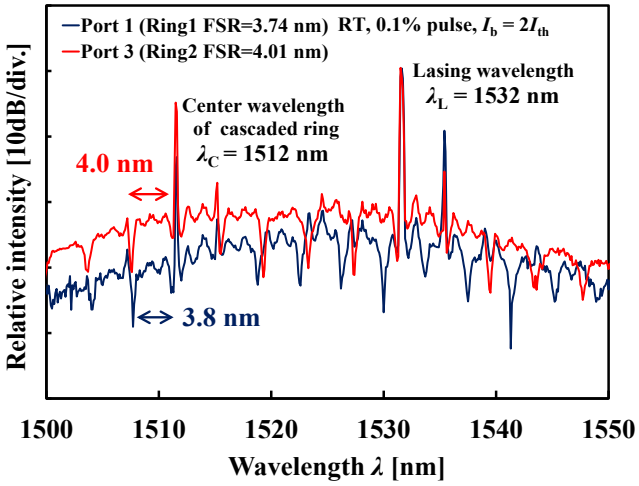

Fig. 9. (Color online) Lasing spectra of output light measured from ports 1 and 2.

cladding and the formation of p/n electrodes were carried out separately using different mask patterns. The details of this process are described in the next section. Finally, Ti/Au electrodes were evaporated on p-GaInAs and n-GaInAsP to form ohmic contacts.

As shown in the cross sectional SEM image of the gain section in Fig. 7, the III–V layer was found to be formed on the Si waveguide without exfoliation even after device fabrication. To measure the characteristics, laser chips were formed by dicing at the Si waveguide edges.

I–L and *I–V* characteristics were measured under room temperature under a pulsed current condition (1 ms period, 0.1% duty), as shown in Fig. 8, where the output powers from ports 1, 2, and 3 were detected simultaneously with a GaInAs photodiode. The length of the gain section and the stripe width of the measured device were 1.0 mm and 9.6 μm, respectively. Note that this device did not have any current confinement structure in order to enable simple fabrication, unlike the device in the simulation in the previous section. As described in the previous section, taper section lengths of 50, 100, and 150 μm were used to observe the effects of taper length on coupling efficiency. The lasing operation was confirmed at a threshold current I_{th} of 66 mA, at which the differential resistance of the *I–V* curve was 8.0 Ω for the device with a taper length of 50 μm. The external differential quantum efficiency η_d (calculated by the sum of powers at ports 1, 2, and 3) was 1.8%, and the output power from each port was confirmed to be almost the same by coupling the output light with a lensed single-mode fiber.

As evident from the *I–L* characteristics, kinks occurred around the threshold current, and the effect was found to be more striking at a larger taper section length ($\eta_d = 2.1\%$ and $I_{th} = 110$ mA for the 100 μm taper section length, and $\eta_d = 1.5\%$ and $I_{th} = 125$ mA for the 150 μm taper section length). We discuss these phenomena in the next section.

The lasing spectra measured by coupling the output light into a lensed fiber are shown in Fig. 9. Through-port characteristics of the ring resonator are superimposed in each spectrum, and measured values of FSR = 3.8 and 4.0 nm are in close accordance with the designed values of 3.74 and 4.01 nm. In addition, we find the center wavelength of the cascaded ring resonator to be 1512 nm, and the periods of the two FSRs are in accordance. However, the output light peak was also seen at 1532 nm, which is the gain peak, because the unnecessary reflection from the taper section or the waveguide edges may not be sufficiently suppressed in this device; therefore, we consider that the suppression of the

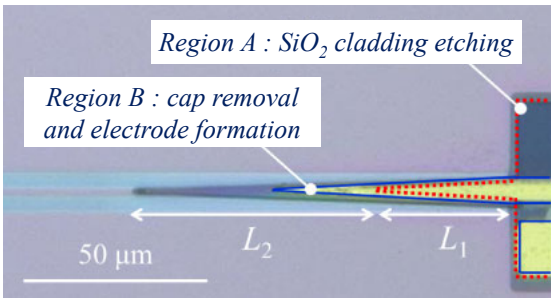

Fig. 10. (Color online) Microscopic view of the taper section. L_1 indicates the electrode length and L_2 the length of the taper section on which electrodes were not formed directly on semiconductor.

reflection must also be investigated to achieve single-mode operation in the future.

4. Discussion

In this section, we discuss how the III–V/Si taper structure affects the *I–L* characteristics. Previous groups so far dealt with the taper structure as a passive device and have mainly investigated the mode coupling characteristics. However, discussion from the perspective of an active device has been insufficient. A situation where current injection into taper section is insufficient for the waveguide to be transparent can cause saturable absorption. In this section, we analyzes kink characteristics by numerical calculation, and propose a novel taper design for eliminating saturable absorption.

As mentioned in the previous section, *I–L* characteristics show kinks around the threshold current. We believe this to be the result of saturable absorption caused by insufficient current injection into the taper section. A microscopic view of the fabricated device (taper length = 100 μm) is shown in Fig. 10.

L_1 indicates the electrode length and L_2 indicates the length of the section where electrodes are not formed directly on the semiconductor. Although the electrode seems to be longer than L_1 in Fig. 10, in reality, the electrode touches the semiconductor layer only in region A because the 1-μm-thick SiO_2 cladding must be dry-etched using a thick photoresist (PR).

The length L_1 was designed to be 30, 60, and 90 μm for taper lengths of 50, 100, and 150 μm, respectively. However, the actual electrode length in the devices was reduced to 18, 40, and 53 μm. The reason for the shrinkage is considered to be the low resolution of photolithography resulting from the use of the 4-μm-thick negative PR in the SiO_2 cladding etching process. The selectivity between SiO_2 and PR is around 1/3, which can be overcome by combining a thin PR with a hard mask.

Figure 11 shows the calculation results for estimating how much current diffuses from the electrode edge into the taper tip. In this calculation, the injection current into the electrode J_t is represented by J_1 and J_2, where J_1 indicates the current component flowing under the electrode, and J_2 indicates the current component diffusing from the electrode edge toward the taper side. In addition, the current diffusion towards the direction of the stripe sidewall is assumed not to occur.

The distribution of current diffusing from the electrode edge to the taper direction (x-direction) in the case of a simple one-dimensional (1D) cross-sectional structure is approximated by[51)]

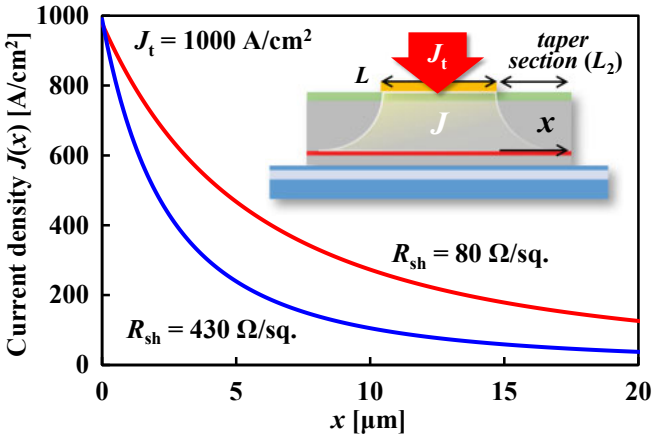

Fig. 11. (Color online) Diffusion current density flowing from electrode edge to taper direction.

$$J(x) = \frac{J_s}{\left(1 + \frac{x}{l_s}\right)^2}, \tag{1}$$

where the saturation current density J_s is given by

$$J_s = \frac{J_t}{1 + \frac{2 \cdot l_s}{L_e}}, \tag{2}$$

J_t being the injection current density. The current diffusion length l_s is given by

$$l_s = \sqrt{\frac{4 \cdot k_B \cdot T}{q \cdot R_s \cdot J_s}}, \tag{3}$$

where L_e, k_B, T, q, R_{sh}, and l_s respectively represent the electrode length, Boltzmann constant, temperature, elementary charge, the sheet resistance of the layer where current flows, and the length at which the amplitude of current density $J(x)$ attenuates by 1/4. Since the hole mobility limits the current diffusion length, the sheet resistance at the current diffusing layer is regarded to be the parallel resistance of the p-GaInAs contact and p-InP cladding layers. The composite sheet resistance R_{sh} is represented as

$$\frac{1}{R_{sh}} = \frac{d_{GaInAs}}{\rho_{GaInAs}} + \frac{d_{InP}}{\rho_{InP}}. \tag{4}$$

Here, ρ and d indicate the resistivity and thickness of each material, respectively. The following values are used in this calculation: $L = 1000\,\mu m$, $d_{GaInAs} = 50\,nm$, $\rho_{GaInAs} = 8.9 \times 10^{-3}\,\Omega{\cdot}cm$ (acceptor density $N_A = 1 \times 10^{19}\,cm^{-3}$, mobility $\mu_{GaInAs} = 70\,cm^2{\cdot}V^{-1}{\cdot}s^{-1}$),[52)] $d_{InP} = 1500\,nm$, $\rho_{IInP} = 8.6 \times 10^{-2}\,\Omega{\cdot}cm$ ($N_A = 1 \times 10^{18}\,cm^{-3}$, $\mu_{InP} = 73\,cm^2{\cdot}V^{-1}{\cdot}s^{-1}$[53)]), $R_{sh} = 430\,\Omega/sq.$, and $T = 300\,K$.

If J_{tr} per QW = $50\,A/cm^2$ and $J_t = 1000\,A/cm^2$ are assumed, the transparent length for 5 QWs is found to be less than $x = 4.8\,\mu m$, as seen in Fig. 11. However, this transparent length is estimated to be improved to 11 μm, if 200-nm-thick p-GaInAs with a carbon concentration of $4 \times 10^{19}\,cm^{-3}$[54)] and 2-μm-thick p-InP are introduced into the laser structure, thereby reducing R_{sh} from 430 to 80 Ω/sq.

Up to now, it had been implied that saturable absorption was caused by insufficient current injection. Now, we consider approximating the kinks found in the *I–L* characteristics by introducing a saturable absorption effect. Excitonic absorp-

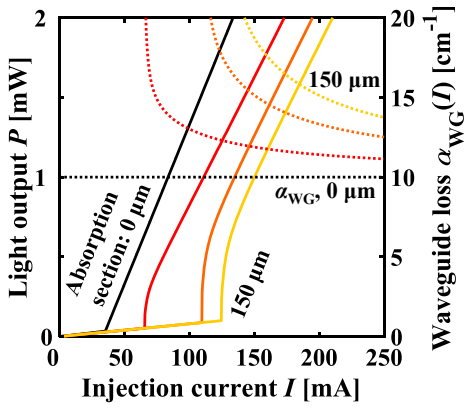

Fig. 12. (Color online) Calculation results of *I–L* characteristic and waveguide loss when assuming saturable absorption effect.

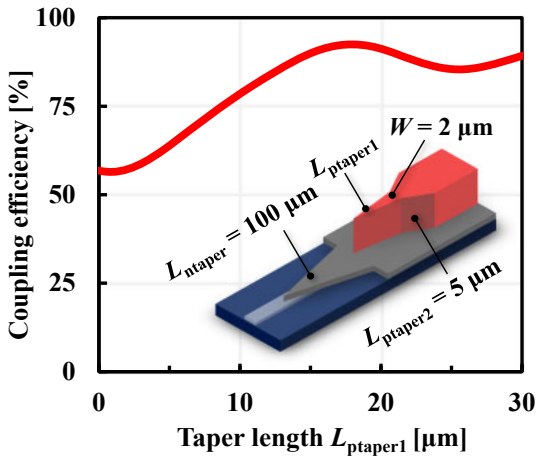

Fig. 13. (Color online) Calculation result of coupling efficiency after introduction of two-step taper.

tion in multiple quantum wells is known to show a high nonlinear optical effect,[55] and the relationship between the incident light intensity P_i and absorption coefficient $\alpha(P_i)$ can be described as

$$\alpha(P_i) = \xi_{taper}\left(\alpha_o + \frac{a_x}{1+\frac{P_i}{P_x}} + \frac{a_b}{1+\frac{P_i}{P_b}}\right), \quad (5)$$

where ξ_{taper}, α_o, α_x, α_b, P_x, and P_b represent the optical confinement coefficient in the taper, the unsaturable background absorption, excitonic absorption that saturates at an optical intensity P_x, and the interband absorption that saturates at the optical intensity P_b, respectively.

We performed a calculation using the following steps. (1) Convert the light output in Fig. 8, $P(I)$, to light intensity shining in the taper section, $P_i(I)$, where $P(I)$ and $P_i(I)$ are functions of the injection current I as in the conversion formula $P_i(I) = \xi_{taper} \cdot P(I)/(W_{act} \cdot D_{act})$. (2) Obtain the absorption coefficient by substituting $P_i(I)$ into Eq. (5). (3) Deliver the equivalent waveguide loss $\alpha_{WG}(I)$ by weighting the original waveguide loss α_{WG} and absorption coefficient $\alpha(P_i)$ in accordance with their length. (4) Calculate η_d and I_{th} using $\alpha_{WG}(I)$ to obtain an *I–L* curve. (5) Adjust the *I–L* curve to the experimental result by finely varying several variables. The approximated *I–L* curves and equivalent absorption coefficient $\alpha_{WG}(I)$ are shown in Fig. 12.

First, we approximated the measurement results with a taper length of 50 µm by setting $\eta_i = 70\%$, $\alpha_{act} = 10\,cm^{-1}$, and $\alpha_{Si} = 3.7\,cm^{-1}$. The propagation loss of a Si waveguide, $\alpha_{Si} = 3.7\,cm^{-1}$, was estimated by referring to the measured value of the Si waveguide patterned on the same substrate as the lasers. At the same time, variables related to the saturable absorption were set to be $\xi_{taper} = 2\%$, $\alpha_o = 600\,cm^{-1}$, $P_x = 125\,W/cm^2$, and $P_b = 4000\,W/cm^2$, where the same values as those in Ref. 42 were used for P_x and P_b. Additionally, approximated curves in the case of various taper lengths can be found to exhibit the same tendency as the experimental values shown in Fig. 8. These results indicate the possibility that the kinks are caused by saturable absorption. Furthermore, when the provided saturable absorption is removed from the taper section, it is found that the threshold current can be reduced by 47% in the case of a taper section length of 50 µm.

In order to eliminate saturable absorption in the taper section, we propose a two-stage taper structure (Fig. 13) that enables us to significantly reduce the p-side taper length and to facilitate current injection into the taper tip. This novel structure is also easily introduced into the current fabrication process because only the modification of the photomask pattern is necessary. The two-stage taper is composed of an n-side lower layer and an upper layer that includes an active region and a p-doped layer. As shown in Fig. 13, the combination of a 100-µm-long n-side taper and a two-stage taper structure on the p-side successfully shortens $L_{ptaper1}$ enough to obtain a high coupling efficiency. L_{1dB} of 10 µm is equivalent to a length of 1/14 compared with that of a conventional structure. This shrinkage of the p-side taper section is expected to suppress the saturable absorption, because the taper length is almost equivalent to the diffusion length of the current.

In addition to the elimination of saturable absorption, given an appropriate ring resonator design (Fig. 6), and the introduction of current confinement, laser performance characteristics of $I_{th} < 20$ mA, $\eta_d > 30\%$, and SMSR > 30 dB can be obtained, as estimated in Sect. 2.

5. Conclusions

We demonstrated a GaInAsP/SOI hybrid laser with a ring-resonator-type reflector fabricated by N_2 plasma-activated bonding. Lasing operation was achieved with a threshold current of 66 mA, and reflective spectra based on the ring resonators were confirmed. We also investigated kink properties that occurred around the threshold current of the *I–L* characteristics, and numerical calculations revealed that the kinks are caused by saturable absorption occurring at the taper tip. By eliminating the saturable absorption and introducing a proper ring design, a highly efficient lasing operation can be expected.

Acknowledgments

This work was supported by JSPS KAKENHI Grant Numbers 15H05763, 25709026, 14J02327, and 15J11774, and by the New Energy and Industrial Technology Development Organization (NEDO), and JST-CREST.

1) N. Farrington, G. Porter, S. Radhakrishnan, H. H. Bazzaz, V. Subramanya, Y. Fainman, G. Papen, and A. Vahdat, Comput. Commun. Rev. **41**, 339 (2011).
2) M. A. Taubenblatt, J. Lightwave Technol. **30**, 448 (2012).
3) K. Hasharoni, S. Benjamin, A. Geron, G. Katz, S. Stepanov, N. Margalit, and M. Mesh, Proc. OFC, 2013, OTu3H.2.
4) K. Hasharoni, S. Benjamin, A. Geron, S. Stepanov, G. Katz, I. Epstein, N. Margalit, and M. Mesh, Proc. SPIE **8991**, 89910C (2014).
5) C. Gunn, IEEE Micro **26** [2], 58 (2006).
6) Y. A. Vlasov, IEEE Commun. Mag. **50** [2], s67 (2012).
7) C. R. Doerr, L. Chen, D. Vermeulen, T. Nielsen, S. Azemati, S. Stulz, G. McBrien, X.-M. Xu, B. Mikkelsen, and M. Givehchi, Proc. OFC, 2014, Th5C.1.
8) R. Soref, IEEE J. Sel. Top. Quantum Electron. **12**, 1678 (2006).
9) B. Jalali and S. Fathpour, J. Lightwave Technol. **24**, 4600 (2006).
10) T. Baba, S. Akiyama, M. Imai, N. Hirayama, H. Takahashi, Y. Noguchi, T. Horikawa, and T. Usuki, Opt. Express **21**, 11869 (2013).
11) J. Fujikata, M. Miura, M. Noguchi, D. Okamoto, T. Horikawa, and Y. Arakawa, Jpn. J. Appl. Phys. **52**, 04CG10 (2013).
12) N. Hatori, Y. Urino, T. Shimizu, M. Okano, T. Yamamoto, M. Mori, T. Nakamura, and Y. Arakawa, Photonics **2**, 355 (2015).
13) Y. Urino, S. Akiyama, T. Akagawa, T. Baba, T. Usuki, D. Okamoto, M. Miura, J. Fujikata, T. Shimizu, and M. Okano, Proc. ECOC, 2013, Mo.4.B.2.
14) S. Kondo, T. Okumura, R. Osabe, N. Nishiyama, and S. Arai, Proc. IPRM, 2010, WeP28.
15) R. Osabe, T. Okumura, S. Kondo, N. Nishiyama, and S. Arai, Jpn. J. Appl. Phys. **50**, 088005 (2011).
16) Y. Hayashi, R. Osabe, K. Fukuda, Y. Atsumi, J. Kang, N. Nishiyama, and S. Arai, Jpn. J. Appl. Phys. **52**, 060202 (2013).
17) J. Suzuki, Y. Hayashi, Y. Kuno, J. Kang, T. Amemiya, N. Nishiyama, and S. Arai, Jpn. J. Appl. Phys. **53**, 118003 (2014).
18) S. B. Yoo, H. J. Lee, Z. Pan, J. Cao, Z. Yanda, K. Okamoto, and S. Kamei, IEEE Photonics Technol. Lett. **14**, 1211 (2002).
19) D. Klonidis, C. T. Politi, M. O'Mahony, and D. Simeonidou, IEEE Photonics Technol. Lett. **16**, 1412 (2004).
20) T. Kita, R. Tang, and H. Yamada, Appl. Phys. Lett. **106**, 111104 (2015).
21) T. Komljenovic, S. Srinivasan, E. Norberg, M. Davenport, G. Fish, and J. E. Bowers, IEEE J. Sel. Top. Quantum Electron. **21**, 214 (2015).
22) N. Kobayashi, K. Sato, M. Namiwaka, K. Yamamoto, S. Watanabe, T. Kita, H. Yamada, and H. Yamazaki, J. Lightwave Technol. **33**, 1241 (2015).
23) H. Wada and T. Kamijoh, IEEE Photonics Technol. Lett. **8**, 173 (1996).
24) K. Matsumoto, X. Zhang, J. Kishikawa, and K. Shimomura, Jpn. J. Appl. Phys. **54**, 030208 (2015).
25) B. Ben Bakir, A. Descos, N. Olivier, D. Bordel, P. Grosse, E. Augendre, L. Fulbert, and J. Fedeli, Opt. Express **19**, 10317 (2011).
26) K. Tanabe, K. Watanabe, and Y. Arakawa, Opt. Express **20**, B315 (2012).
27) K. Tanabe and Y. Arakawa, Proc. CLEO, 2014, STh1G.6.
28) T. Creazzo, E. Marchena, S. B. Krasulick, P. K. Yu, D. Van Orden, J. Y. Spann, C. C. Blivin, L. He, H. Cai, and J. M. Dallesasse, Opt. Express **21**, 28048 (2013).
29) Y.-H. Jhang, K. Tanabe, S. Iwamoto, and Y. Arakawa, IEEE Photonics Technol. Lett. **27**, 875 (2015).
30) A. W. Fang, H. Park, O. Cohen, R. Jones, M. J. Paniccia, and J. E. Bowers, Opt. Express **14**, 9203 (2006).
31) A. W. Fang, E. Lively, Y.-H. Kuo, D. Liang, and J. E. Bowers, Opt. Express **16**, 4413 (2008).
32) A. W. Fang, B. R. Koch, R. Jones, E. Lively, D. Liang, Y.-H. Kuo, and J. E. Bowers, IEEE Photonics Technol. Lett. **20**, 1667 (2008).
33) D. Liang, M. Fiorentino, T. Okumura, H.-H. Chang, D. T. Spencer, Y.-H. Kuo, A. W. Fang, D. Dai, R. G. Beausoleil, and J. E. Bowers, Opt. Express **17**, 20355 (2009).
34) C. Zhang, S. Srinivasan, Y. Tang, M. J. Heck, M. L. Davenport, and J. E. Bowers, Opt. Express **22**, 10202 (2014).
35) G. Roelkens, D. Van Thourhout, R. Baets, R. Nötzel, and M. Smit, Opt. Express **14**, 8154 (2006).
36) S. Stankovic, R. Jones, M. N. Sysak, J. M. Heck, G. Roelkens, and D. Van Thourhout, IEEE Photonics Technol. Lett. **24**, 2155 (2012).
37) M. Lamponi, S. Keyvaninia, C. Jany, F. Poingt, F. Lelarge, G. de Valicourt, G. Roelkens, D. Van Thourhout, S. Messaoudene, and J.-M. Fedeli, IEEE Photonics Technol. Lett. **24**, 76 (2012).
38) S. Keyvaninia, G. Roelkens, D. Van Thourhout, C. Jany, M. Lamponi, A. Le Liepvre, F. Lelarge, D. Make, G.-H. Duan, and D. Bordel, Opt. Express **21**, 3784 (2013).
39) S. Tanaka, S. Jeong, S. Sekiguchi, T. Kurahashi, Y. Tanaka, and K. Morito, Opt. Express **20**, 28057 (2012).
40) T. Maruyama, T. Okumura, and S. Arai, Jpn. J. Appl. Phys. **45**, 8717 (2006).
41) T. Maruyama, T. Okumura, S. Sakamoto, K. Miura, Y. Nishimoto, and S. Arai, Opt. Express **14**, 8184 (2006).
42) T. Okumura, T. Maruyama, H. Yonezawa, N. Nishiyama, and S. Arai, IEEE Photonics Technol. Lett. **21**, 283 (2009).
43) A. Karim, K. Black, P. Abraham, D. Lofgreen, Y. Chiu, J. Piprek, and J. Bowers, IEEE Photonics Technol. Lett. **12**, 1438 (2000).
44) X. Sun, M. J. Shearn, A. Zadok, M. S. Leite, S. T. Steger, H. A. Atwater, A. Scherer, and A. Yariv, Proc. CLEO, 2010, CTuO6.
45) G. Kurczveil, P. Pintus, M. J. Heck, J. Bowers, and J. Peters, IEEE Photonics J. **5**, 6600410 (2013).
46) D. K. T. Ng, Q. Wang, J. Pu, K. P. Lim, Y. Wei, Y. Wang, Y. Lai, and S. T. Ho, Opt. Lett. **38**, 5353 (2013).
47) J. Pu, V. Krishnamurthy, D. K. T. Ng, K. P. Lim, C.-W. Lee, K. Tang, A. Y. S. Kay, T.-H. Loh, F. Tjiptoharsono, and Q. Wang, IEEE J. Sel. Top. Quantum Electron. **21**, 1501808 (2015).
48) M. Yamada and Y. Suematsu, IEEE J. Quantum Electron. **15**, 743 (1979).
49) N. Nunoya, M. Nakamura, M. Morshed, S. Tamura, and S. Arai, IEEE J. Sel. Top. Quantum Electron. **7**, 249 (2001).
50) H. Takagi, K. Kikuchi, R. Maeda, T. Chung, and T. Suga, Appl. Phys. Lett. **68**, 2222 (1996).
51) H. Yonezu, I. Sakuma, K. Kobayashi, T. Kamejima, M. Ueno, and Y. Nannichi, Jpn. J. Appl. Phys. **12**, 1585 (1973).
52) C. Chellic, D. Cui, S. M. Hubbard, A. Eisenbach, D. Pavlidis, S. K. Krawczyk, and B. Sermage, Proc. IPRM, 1999, MoP16.
53) M. Sotoodeh, A. Khalid, and A. Rezazadeh, J. Appl. Phys. **87**, 2890 (2000).
54) Z. Griffith, E. Lind, M. J. W. Rodwell, X.-M. Fang, D. Loubychev, Y. Wu, J. M. Fastenau, and A. W. K. Liu, Proc. IPRM, 2007, WeA3-2.
55) A. Fox, A. Maciel, M. Shorthose, J. Ryan, M. Scott, J. Davies, and J. Riffat, Appl. Phys. Lett. **51**, 30 (1987).